Journal of the European Ceramic Society 39 (2019) 3247–3256

Contents lists available at ScienceDirect

Journal of the European Ceramic Society

journal homepage: www.elsevier.com/locate/jeurceramsoc

Nanoindentation-based study of the mechanical behavior of bulk supercrystalline ceramic-organic nanocomposites

Büsra Bor[a], Diletta Giuntini[a], Berta Domènech[a], Michael V. Swain[b,c], Gerold A. Schneider[a,*]

[a] Institute of Advanced Ceramics, Hamburg University of Technology, Denickestrasse 15, D-21073, Hamburg, Germany
[b] Department of Aerospace, Mechanical and Mechatronic Engineering, University of Sydney, J07, Sydney, NSW, 2006, Australia
[c] Biomaterials Engineering, Don State Technical University, Rostov-on Don, 344000, Russia

ARTICLE INFO

Keywords:
Supercrystalline material
Nanocomposite
Mechanical behavior
Nanoindentation
Fracture toughness

ABSTRACT

Bulk poly-supercrystalline ceramic-organic nanocomposites were produced and characterized with a nanoindentation-based study. These nanocomposites were processed using two different routines, to compare their properties with and without crosslinking the organic ligands interfacing the ceramic nanoparticles. Together with the expected material strengthening induced by crosslinking, a distinct response emerges when using Berkovich and cube-corner indenters. The supercrystalline materials are prone to compaction, cracking and chipping phenomena that become more severe when a sharper tip is employed, implying that a Berkovich indenter is more suitable for the evaluation of elastic modulus and hardness. The cube-corner tip, on the other hand, is employed for the investigation of fracture toughness, comparing two methods and multiple models available from the literature. The fracture toughness outcomes suggest that cracks evolve with a quarter-penny shaped profile at the indent's corners, and that extrinsic toughening mechanisms, such as plastic-like deformation and crack deflection, play a significant role.

1. Introduction

Supercrystalline materials are a rising field of attention in materials science and nanoengineering. They consist of nanoparticles organized into ordered structures, typically called superlattices, referred into literature as supercrystals [1,2] or mesocrystals [3,4]. The supercrystals' superlattice structure depends on the nature and shape of the nanoparticles themselves, and it is often analogous to conventional crystalline ones, such as face-centered cubic, hexagonal close packed, and so on. The nanoparticles that constitute the superlattices can in turn be crystalline (nanocrystals), and usually they are surface-functionalized with organic ligands. The arrangement of these functionalized nanocrystals into supercrystalline materials results in a variety of interesting electronic, magnetic, optical, thermal and mechanical properties. Their applications, already established or still in their infancy, range between energy storage materials, battery electrodes, catalysts, sensors, solar cells, optoelectronics, and biomedical products [3–6]. These self-assembled organic-inorganic nanocomposites also have considerable potential for the development of bioinspired materials with enhanced mechanical properties. In the last few decades, significant efforts have been made to reproduce the features of natural materials that render them so attractive for structural purposes: a unique combination of strength, hardness, stiffness and fracture toughness. These characteristics are the result of complex architectures, in which nanoscale inorganic building blocks, interfaced by a minimal amount of soft organic matrix, are arranged into multi-level hierarchical structures [7–13]. Supercrystalline materials offer the possibility of combining the main prerequisites needed for the smallest hierarchical levels, namely the utilization of nanoscale building blocks (characterized by strength values approaching theoretical ones), tight packing of the inorganic phase and good control over the organic matrix content. Tailoring such superlattice parameters has proven to be a successful route towards the production of ceramic-organic nanocomposites with substantial strength, stiffness and hardness, among the highest reported for these types of materials [14].

Supercrystalline materials are nevertheless still unavailable in bulk 3-D form. They are typically thin films, or, when three-dimensional, their size does not exceed a few hundreds of microns in the best cases. Their mechanical properties have also just started to be thoroughly investigated, and are generally associated with large experimental data scatter [15,16]. Several interesting aspects of the mechanical response of 3-D supercrystalline materials, at least at the microscale, have

* Corresponding author.
E-mail addresses: buesra.bor@tuhh.de (B. Bor), diletta.giuntini@tuhh.de (D. Giuntini), berta.domenech@tuhh.de (B. Domènech), michael.swain@sydney.edu.au (M.V. Swain), g.schneider@tuhh.de (G.A. Schneider).

https://doi.org/10.1016/j.jeurceramsoc.2019.03.053
Received 15 January 2019; Received in revised form 22 March 2019; Accepted 23 March 2019
Available online 25 March 2019
0955-2219/ © 2019 The Authors. Published by Elsevier Ltd. This is an open access article under the CC BY-NC-ND license (http://creativecommons.org/licenses/BY-NC-ND/4.0/).

nevertheless started to emerge. These include how the close-packed arrangement of the nanoparticles allows a homogeneous stress distribution within the material with respect to amorphous nanocomposites [15], the importance of the degree of ordering towards the enhancement of hardness and elastic modulus [2,17], the limited influence of the nanoparticles' size on the material's stiffness [18], the role of the supercrystals growth mechanisms on the final properties [19], and the effect of the superlattice defects induced by residual solvent trapped during the self-assembly process [20].

A typical method of choice for the assessment of the mechanical properties of supercrystalline materials is nanoindentation, either using atomic force microscopy (pN to a few tens of mN loads) or, more commonly, with nanoindenters (up to 500 mN). Alternative approaches include buckling of self-assembled thin films [16] and a SAXS study of 3-D supercrystalline domains under quasi-hydrostatic pressure [21]. The use of nanoindentation testing methods can be applied not only to the measurement of the material's elastic modulus and hardness, but also to the evaluation of its fracture toughness and constitutive behavior [22–25]. The applicability of traditional nanoindentation procedures to supercrystalline materials needs, however, to be treated with caution, as several uncertainties using traditional testing procedures have already emerged [26–29], such as difficulties in estimating the material's contact stiffness from nonlinear loading and unloading curves, plus possible errors in indentation load recordings due to the device-imposed oscillations. Supercrystalline materials also present the additional unconventional feature of having characteristic lattice parameters in the nm range.

In the present work, nanoindentation measurements are used for the evaluation of the mechanical properties of bulk, three-dimensional, macroscopic supercrystalline materials, constituted of iron oxide nanoparticles functionalized with a monolayer of oleic acid. This specific material system has been recently utilized for the design of a routine to produce bulk supercrystalline nanocomposites, with excellent results in terms of final strength, stiffness and hardness, thanks to the option of inducing the oleic acid molecules to crosslink [14]. Up to this point, nanoindentation has been used on these materials to routinely measure their elastic modulus and hardness, by means of a Berkovich tip penetrating typically 2000 nm depth into the material [14]. Here, nanoindentation using both Berkovich and cube-corner indenters with a range of indenter loads, is instead utilized as a tool for a more thorough analysis of the material's response to various degrees of mechanical deformations. The effects of different nanoindentation tips and analysis methods are assessed for the materials both prior to and after crosslinking. The recorded load-displacement curves are analyzed with the aid of direct SEM observations of the indents, in order to gain a better understanding of the supercrystals' deformation and failure behavior. The material's fracture toughness is also estimated, with two different methods, the classic indentation crack length method (ICL) and an energy-based approach, to add to the evaluation's reliability and account for the different cracking mechanisms around the indentation sites. Quantitative analysis of the obtained fracture toughness data is performed with a Barrenblatt crack-tip closure approach [30]. The different mechanical responses of supercrystalline materials with and without crosslinking of the organic phase are then critically discussed.

2. Materials and methods

The basic constituents of the supercrystalline materials are iron oxide (magnetite, Fe_3O_4) nanoparticles with a diameter of 18.4 ± 0.2 nm and functionalized with oleic acid ($C_{18}H_{34}O_2$, 11%wt.), produced by CAN GmbH (Hamburg, Germany). The functionalized nanoparticles are initially suspended in toluene. The process to obtain bulk supercrystalline pellets consists of three steps: self-assembly, pressing and heat treatment. The self-assembly method chosen was solvent destabilization by slow diffusion of a non-solvent. This method consists of adding to the suspension a second solvent, which is miscible with the starting suspension, but is a poor solvent medium for the functionalized nanoparticles. The "non-solvent" has a destabilization effect, promoting gradual clustering of the nanoparticles in suspension, in such a way that they slowly arrange themselves in tightly packed supercrystalline structures [5]. In the present case, ethanol was chosen as destabilizing agent.

The samples were prepared by pouring the starting suspension, with a concentration of 240 g/L of functionalized nanoparticles in toluene, inside dies with an internal diameter of 14 mm. The dies were then placed into a sealed desiccator with atmosphere enriched in ethanol. The self-assembly process lasted 15 days. At the end of these 15 days, the dies were extracted from the desiccator, the remaining solvent was removed, and vacuum drying was performed. The resulting samples were then in the form of mainly supercrystalline grains in a face-centered cubic (FCC) structure sedimented at the bottom of the dies. The subsequent step was the shaping of the sedimented material into cylindrical pellets, which was achieved by means of uniaxial pressing (50 MPa at 150 °C). The samples in this state are subsequently referred to as-pressed (AP). A final processing step was the heat treatment of as-pressed samples, performed under N_2 (g) at 325 °C, with a holding time of 18 min, and 1 °C/min heating and cooling ramps. These samples are denoted as heat-treated (HT). All processing parameters were empirically optimized in a previous study [14]. Fig. 1 shows a typical supercrystalline nanostructure for an iron oxide-oleic acid nanocomposite after pressing. Heat treatment does not alter such a nanostructure [14], but it is of utmost importance in order to obtain a strong and stiff material. The applied heat energy covalently crosslinks the oleic acid ligands, thus bridging the nanoparticles, and leading to a 3- or 4-fold increase in the nanocomposites' strength, stiffness and hardness. A critical appraisal of such a dramatic boost of the material's mechanical properties was among the objectives of the present study, and therefore each sample was cut into two portions. One was left as-pressed (AP), while the other was heat-treated (HT) using the procedure described above, in order to more thoroughly compare their mechanical properties and behavior.

Once the samples had been manufactured (typical size 14 mm in diameter and 4 mm in thickness), they were prepared for nanoindentation. Portions of each sample were selected, such that the indented surface was the samples' cross-section implying that the indentation load was applied perpendicular to the compaction axis. They were then embedded into cold-curing acrylic mounting resin (Scandiquick, Scan-DIA, Hagen, Germany). The samples' surfaces were polished with silicon carbide papers of decreasing roughness, and finally with diamond suspensions with characteristic sizes starting from 15 μm down to 50 nm. The final surface roughness was consistently lower than 30 nm for the AP material and of 20 nm for the HT material.

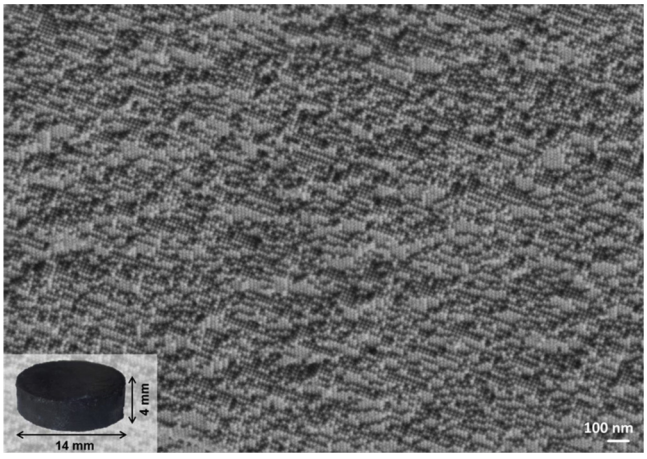

Fig. 1. SEM image of the nanostructure of a supercrystalline material, as-pressed (AP) and inset of a photograph of a typical 14 mm-diameter AP pellet.

The nanoindentation tests were carried out at room temperature with an Agilent Nano Indenter G200 (Agilent, Santa Clara, CA, USA). In order to investigate the nanocomposite material's mechanical behavior more in detail, two indentation tips were used: Berkovich (B) and cube-corner (CC). The latter is characterized by a more acute face angle (35.26° instead of 65.27°), creating sharper indents in the material, and thus inducing more severe stress concentration and cracking phenomena. The Berkovich tip is ideally suited for the evaluation of the nanocomposites' elastic modulus and hardness, while the cube-corner for the estimation of its fracture toughness.

The continuous stiffness measurement (CSM) mode was applied [31], with a harmonic displacement target of 2 nm and a harmonic frequency of 45 Hz. The nanoindenter operated in displacement control mode with a 0.05 s^{-1} strain rate target and a 10 s hold at the maximum depth. The materials' Poisson's ratio was assumed to be 0.3. Five different indentation depths were used: 300, 500, 700, 1000 and 2000 nm. Fifteen indents per depth were performed, separated from each other by a 30 μm gap.

All indents were subsequently observed in a scanning electron microscope (SEM Zeiss SUPRA 55-VP, Zeiss, Germany), in order to verify that they had been performed in defect-free supercrystalline areas, and to better visualize the deformation mechanisms of the nanocomposites. These micrographs were further processed with image analysis software (ImageJ) [32], in order to measure the parameters necessary for the data post-processing (indent area, radial crack length and chip extension).

3. Results and discussion

3.1. Hardness and elastic modulus

SEM images of the residual nanoindentation impressions are shown in Fig. 2 for the Berkovich as well as cube-corner indenters. Interestingly, the indents in the AP material show signs of material removal at their edges, which has probably adhered to the indenter tip and subsequently been detached from the sample's surface, because of the weak bonding between the functionalized nanoparticles. The incidence of this effect is reduced for the cube-corner indents in the AP material, and never observed in the HT samples, in which the organic molecules' crosslinking appears to prevent such material removal. In the HT material, cracks already appear at the shallowest impression depths (300 nm), while chipping starts occurring at greater depths.

On the other hand, in the AP material, even for 300 nm-deep indents one can identify the peculiar material removal mentioned above, corresponding to just a few layers of nanoparticles along the indenter faces close to edge of contact. Note also that this material removal has a different appearance with respect to what is normally defined as chipping around indents in ceramics. In the latter case, portions of material adjacent to the indents' edges detach from the bulk, due to shear stresses and interactions between radial cracks. In the case of the AP samples' shallow indents, decohesion of the material only requires very low tearing loads, likely due to the nanoparticles rearrangement and adhesion to the Berkovich tip. It is worth mentioning explicitly here that, as mentioned in the paragraph above, the AP material had a slightly more marked surface roughness than the HT one, in line with the easiness of nanoparticles removal in the two cases. This leads to the different appearance of the two materials' surfaces, accompanied by the fact that two different SEMs were used to image them.

Typical load-displacement curves are shown in Fig. 3, revealing the AP and HT material response when indented in CSM–mode at the various depths with Berkovich and cube-corner indenters. The load-displacement curves with increasing maximum depth follow the same loading path for both the AP and HT material, with only slight variations associated with differences between indented surface areas. Once the permanent deformation of the material has started, in the loading curves of both AP and HT materials, several sudden changes of slope (so-called pop-in events, marked on the figure with arrows) can be identified. These pop-in events can result from dislocation activity, slip, twinning, cracking or chipping events. With the information gained from the images in Fig. 2 we interpret these pop-ins as the formation of cracks first, and chipping events immediately thereafter, while we assume that the material removal described above for the AP material happens during unloading [33,34]. As expected, with increasing indentation depth more pop-in events occur.

At the end of the loading curve, the applied load is held constant for 10 s, during which further displacement occurs, indicating that the materials are undergoing creep (marked in the insets of Fig. 3), which were more severe in the AP material than in the HT. The creep effect is still visible in the initial stages of the unloading curve, where one can observe the displacement remaining constant even after the tip has started to retract. The unloading then proceeds as expected, with a relatively minor elastic recovery portion with respect to the permanent deformation. The apparent pop-out effect detected during the unloading path of each indentation curve at 10% of the maximum load occurs because of an additional hold imposed by the device to determine the thermal drift correction.

Fig. 4 shows the measured elastic modulus and hardness relative to cube-corner and Berkovich tips, respectively, for both AP and HT nanocomposites. For the AP samples the elastic modulus is independent of the indentation depth. This is expected as the elastic modulus is a constant by definition. However, the modulus obtained from the cube-corner indents is twice that of the Berkovich indents, which is surprising in view of the pronounced cracking of the AP samples indented with a cube-corner tip.

Based upon the results in Fig. 4 the elastic response of the AP nanocomposites is very sensitive to the shape of the indenter in the CSM-mode. Even though the indenter probes the elastic response of the whole underlying half space, the main contribution comes from a half space with characteristic dimensions that scale with the size of the indent. As observable in Fig. 2, the shallow Berkovich indentation imprint is almost two times bigger in edge length than a cube-corner indent for the same depth. Therefore, the Berkovich indenter probes a volume approximately 8-times bigger than the cube-corner. The nanoparticles' displacements in an 8-times bigger half-space are also smaller, because the Berkovich indenter distributes the load over a wider area with respect to the sharp cube-corner indenter. This leaves ample space for the weakly-connected nanoparticles to accommodate the deformation imposed by the Berkovich tip. Furthermore, the cube-corner tip produces very high local stresses which may lead to additional densification of the material. Fig. 5 provides a visual representation of this effect. Therefore, we assume that the true value of the elastic modulus of the AP material is measured by the Berkovich indenter, whereas the cube-corner tip measures the response of a locally densified material.

The heat-treated samples show much higher values of elastic modulus for both indenter shapes, but in addition they indicate a strong decrease in modulus with indentation depth. The Berkovich values are higher than the cube-corner values, the opposite behavior with respect to the AP samples. The general trend of an increase of the nanocomposites' stiffness with heat treatment is, as expected, due to the thermally-induced crosslinking of the oleic acid molecules, which are in turn anchored to the iron oxide nanoparticles. The covalent crosslinking corresponds to the opening of the double bond in the oleic acid chain, and further formation of a carbon-carbon single bond between two adjacent oleic acid aliphatic chains, which increases bonding of the nanoparticles in their positions, limiting their sliding and rearrangement ability [14]. We attribute the difference in the elastic moduli determined with the two indenters to cracking and chipping induced in the samples, which are more pronounced for the cube-corner indenter than the Berkovich. We therefore conclude that the true elastic modulus is again that determined using the Berkovich indenter. Note that the two different half spaces probed by Berkovich and cube-corner tips, together with the stress concentration-induced additional damage

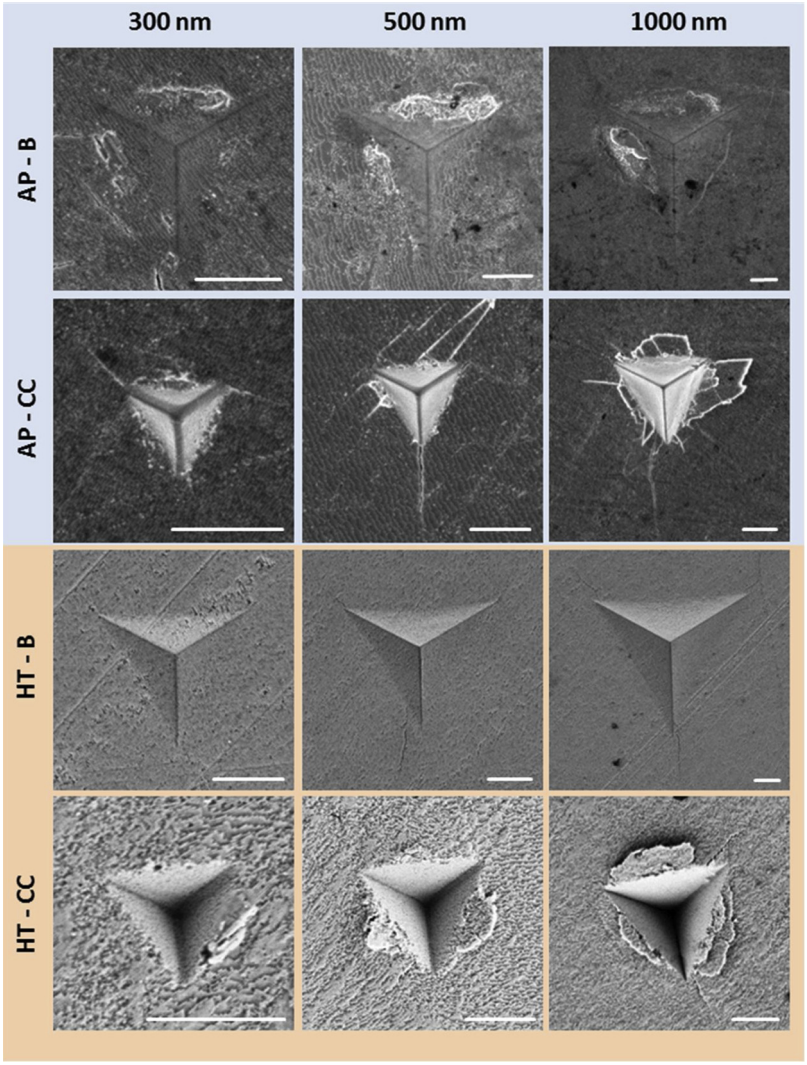

Fig. 2. SEM images of typical Berkovich (B) and cube-corner (CC) indents in AP and HT nanocomposites with the respective indentation depths given at the top of the rows. The higher resistance of the HT material is reflected into the smaller indented areas with respect to their AP counterparts at the same indentation depths, less severe cracking and chipping damage, and absence of material removal at the edges of B-indents. Scale bar is 1 μm in all micrographs.

phenomena associated with the cube-corner tip, are also responsible for the large disparities in maximum indentation loads applied with the two tips for the same penetration depths.

The hardness measurements show the same qualitative trend in regard to the influence of the indenter tip on the two samples. For the HT material there is a pronounced decrease in elastic modulus and hardness with the indentation depth. As both these values decrease, an indentation size effect based on geometrically necessary dislocations cannot be obviously inferred. The hardness decrease with indentation depth is instead attributed to the increasingly more severe damage processes, such as cracking and chipping, which appear with higher applied loads. These damage phenomena influence both elastic modulus and hardness, and thus lead to the detected size effect in the HT material.

We thus attribute the variations in elastic modulus and hardness with indentation depth to distinct phenomena depending on the amount of organic ligands and their crosslinking. In the AP case, the ligands are not crosslinked and the nanoparticles interact *via* van der Waals forces and steric interaction of the ligands. Due to these weak interactions, the ligands can be compressed under the indenter's applied load. In addition, a deformation of the supercrystalline lattice is possible by nanoparticles rearrangement, inducing point defects or dislocations-like structures, as a follow-up study will show. Because of these mechanisms, material compaction under the indenter's tip leads to constant or slightly increasing E and H values in the AP materials, especially under cube-corner indenter. In the HT nanocomposites, on the other hand, the ligands are crosslinked with covalent bonds, making the material much stiffer and harder, but also brittle. Therefore, cracking and chipping phenomena dominate the material's response, resulting in a reduction of hardness and elastic modulus with increasing indentation depths. These considerations are summarized in Fig. 5. Because of such a pronounced effect of material compaction and damage on the measured mechanical properties already starting at shallow indentation depths, the representative values of hardness and elastic modulus are selected to be the ones recorded at 300 nm, for both AP and HT material. Therefore, we have $E = 14.8 \pm 1.1$ GPa and $H = 0.60 \pm 0.08$ GPa for the AP material, and $E = 64.1 \pm 5.8$ GPa and $H = 4.72 \pm 0.62$ GPa for the HT material.

As a consequence of the observed cracking and chipping phenomena, an additional verification of the measured hardness values was performed by utilizing directly the definition of hardness itself, namely:

$$H = \frac{P_{max}}{A} \tag{1}$$

where P_{max} is the maximum indentation load (N), and A is the corresponding projected surface area of the indents, measured on SEM

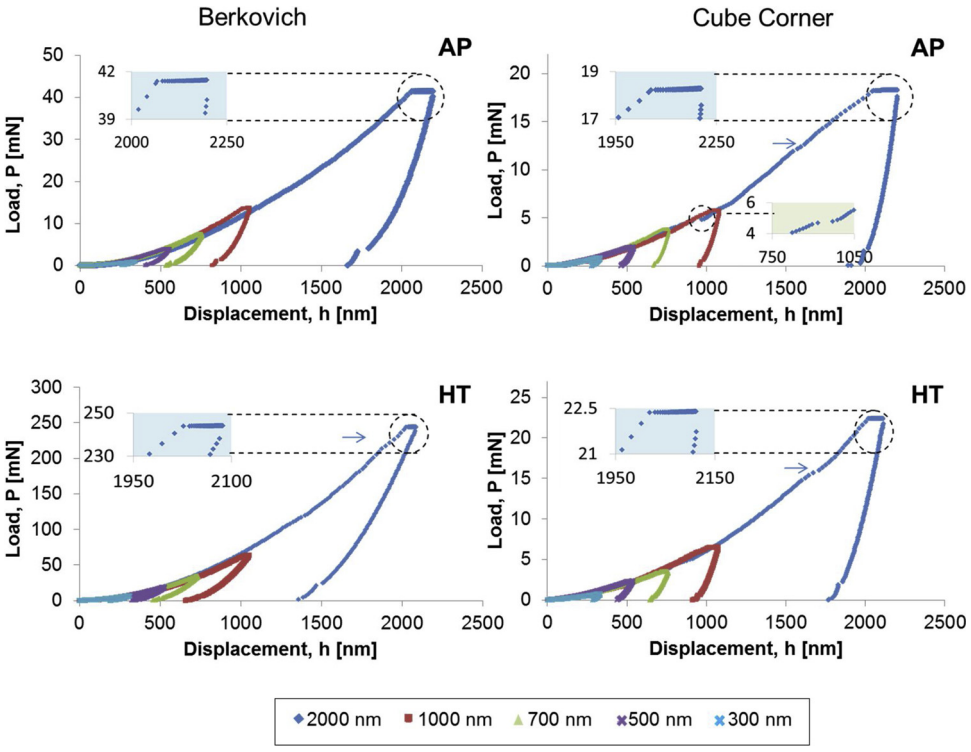

Fig. 3. Nanoindentation load-displacement curves for AP and HT materials with a Berkovich (left) and cube-corner (right) indenters loaded in the CSM-mode. Arrows mark pop-in events, which correspond to cracking and chipping phenomena.

micrographs with the aid of image analysis software (ImageJ). This hardness recalculation method was applied to all the Berkovich indents free of chipping and cracking damage. As Table 1 shows, good agreement is found at 300 nm depth between this and the CSM method, compatibly with the large data scatter that typically affects supercrystalline materials. The slightly lower average hardness values characterizing the image analysis method can be attributed to a possible relaxation of the material, as the SEM images were taken several days after nanoindentation was performed. As displayed in Fig. 3, the material shows creep behavior, both in AP and HT conditions.

The hardness derived *via* image analysis method was subsequently used to recalculate the load-displacement curves for the two materials, when the materials were assumed to exhibit purely elastoplastic behavior, that is in the absence of cracking and chipping damage and neglecting the material's compaction under the indenter. Such curves will also be utilized in the next section for the study of the material's fracture toughness.

The purely elastoplastic curves were reconstructed by taking indentation depth (displacement, x-axis) steps of 1 nm. At each of these steps, the indented area was independently calculated using fused silica and fitted with the well-known calibration function for a Berkovich tip, namely $A_c = 24.5h_c^2 + 49.53h_c + 0.9985h_c^{\frac{1}{2}} + 0.9967h_c^{\frac{1}{4}}$. A_c is the calibrated area and h_c is the contact depth [35]. The indentation load corresponding to each 1-nm displacement step was then determined as $P = H \bullet A_c$, until the maximum load value P_{max} recorded with the CSM method was reached. As stated above, H here is the hardness obtained *via* image analysis method, with the underlying assumption that its value does not change with indentation depth (as we are ruling out cracking and chipping phenomena).

Fig. 6 shows two examples of reconstructed elastoplastic curves for the Berkovich indenter compared to the corresponding experimental CSM ones, for AP and HT materials. As expected, the two curves diverged more significantly for the AP material, which was affected more severely by cracking and chipping damage. The work of deformation associated with both purely elastoplastic and total deformations are also marked in Fig. 6, as $U_{e/p}$ and $U_{measured}$, respectively.

3.2. Fracture toughness

The fracture toughness of the two supercrystalline materials, AP and HT, was evaluated using two methods: indentation crack length method (ICL) and an energy-based work of fracture method. Both these methods rely on nanoindentation measurements, which probe only volumes up to the μm-scale. As supercrystalline grains are typically several tens of μm in size, the measured fracture toughness is representative of the resistance to crack propagation of single supercrystals. The indents for the fracture toughness study were specifically selected in the SEM to be the ones located in areas with homogeneous superlattice orientation. Preliminary observations of the material under the indents (unpublished) show that supercrystallinity is typically uniform for several tens of μm in depth too. If one were to use micro- or macro- (Vickers) indenters, the effect of inter-supecrystalline boundaries would also be included, most likely leading to higher values of fracture toughness, thanks to extrinsic toughening effects like grain boundary deflection, frictional sliding or even crack bridging.

For the ICL method, the indents produced with a cube-corner tip were used, since with such a sharper tip cracking is induced at lower forces. There are two types of equations available in the literature for the calculation of fracture toughness *via* ICL method on indents obtained with cube-corner tip [36–39]. The selection of the most suitable equation depends on the crack path evolution (so called "half-penny" or "Palmqvist" cracks) under the indents [40]. As the latter feature is unknown for our bulk ceramic-organic supercrystalline materials, both types of equations were employed and their outcomes subsequently compared.

If a half-penny crack configuration is assumed, Eq. (2) is utilized, as suggested by Anstis et al. [36]

$$K_{Ic} = \alpha\left(\frac{E}{H}\right)^{1/2}\frac{P}{c^{3/2}} \quad (2)$$

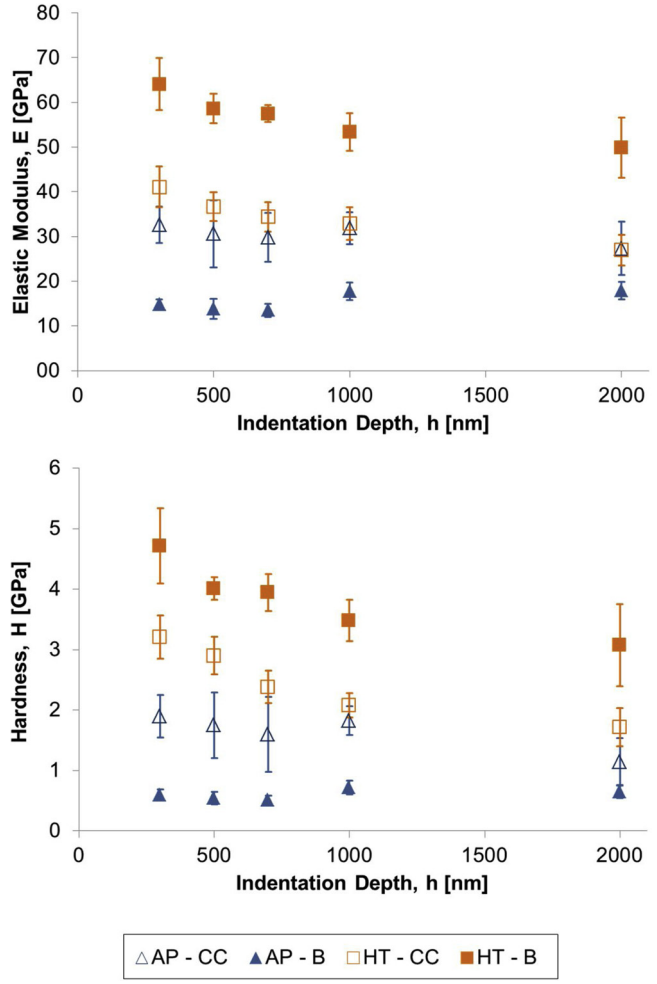

Fig. 4. Elastic modulus and hardness of as-pressed (AP) and heat-treated (HT) materials, tested with Berkovich (B) and cube-corner (CC) tips.

where P is the indentation load and c is the mean overall crack length starting from the center of the indents. The values of E and H are the values measured at 300-nm depth with Berkovich tip. The empirical constant α, depending on the geometry of the indenter and the crack morphology, was estimated with the method developed by Scholz et al. for cube-corner tips [41]. This allows Eq. (2) to be adapted from the case of Vickers to cube-corner indenter tips, and thus to compensate for the inapplicability of the half-penny crack configuration for a three-sided indenter. They showed that α varies with the crack length/indent size (c/a) ratio, as

$$\alpha = 0.0211\left(\frac{c}{a}\right)^{0.3785} \tag{3}$$

where a is the distance between the center and the tip of the indent. The most typical value for α in the literature ranges between 0.036 and 0.040 [22,42,43]. On the other hand, additional studies [44] have shown that by fitting the fracture toughness Eq. (2) to experimental values of E, H, P, c and K_{Ic}, a value of $\alpha = 0.026 \pm 0.001$ should be adopted for cube-corner indenters. This wide range of α values is due to this parameter's dependence on the ratio between crack length and indent size (c/a), which Scholz et al. summarized with Eq. (3). In the present work, we are in the low c/a ratio regime, and α was thus found to be 0.024 ± 0.001. The crack lengths were evaluated as depicted in Fig. 7. In case of the absence of a crack at one of the corners of the indents, the values of a and c were considered to be coincident. In the case of multiple radial cracks stemming from the same corner, the average value was used for the crack length of the corresponding corner.

If, instead, a Palmqvist crack configuration is assumed, the equation proposed by Laugier [37] is used, namely:

$$K_{IC} = k^p\left(\frac{a}{l}\right)^{1/2}\left(\frac{E}{H}\right)^{2/3}\frac{P}{c^{3/2}} \tag{4}$$

Here l is the crack length starting from the corner of the indents and k^p is an empirical constant for the indenter geometry, estimated as 0.015 by Laugier for four-sided Vickers indenters. Again, in order to modify this empirical constant for the case of three-sided cube-corner indenters, Cuadrado et al. [44] fitted k^p to existing K_{Ic} experimental data, and found $k^p = 0.057 \pm 0.002$ for Eq. (4). They also showed, through focused ion beam (FIB) tomography, that for materials with low toughness the crack morphology under cube-corner indents is usually of the quarter-penny shape [45].

Note that, for the ICL method, only indents that did not show any chipping phenomena were used, which limited the analysis to 300, 500 and 700 nm-deep indents. Since chipping starts occurring from 500 nm indentation depth for both AP and HT materials, a selection of the indents based on SEM micrographs was performed. Table 2 shows the obtained values of K_{Ic} for as-pressed and heat-treated material with the two equations, (2) and (4). The reinforcement of the material induced by the oleic acid molecules' crosslinking leads to an almost 2-fold

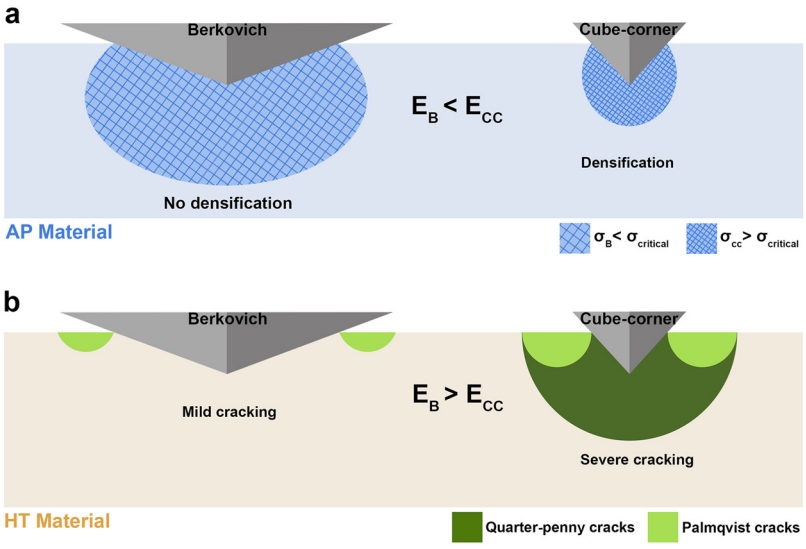

Fig. 5. Schematics of nanoindentation-probed volumes and resulting densification and cracking phenomena for the two indentation tips. We assume that in the AP material (a) as the ligands are not crosslinked the material can be densified if a critical stress level $\sigma_{critical}$ is met. Thus, the high and very localized stresses induced by the cube-corner tip σ_{cc} lead to material densification, while the shallower Berkovich tip does not produce stresses σ_B high enough for densification. In the HT material (b), the crosslinked ligands lead to a brittle material which reacts by more severe cracking by the sharper cube-corner indenter with respect to the Berkovich indenter. Whether there are Palmqvist or half-penny shaped cracks underneath the cube-corner indenter should be studied for instance by FIB-tomography.

Table 1
Comparison of the hardness values obtained *via* CSM and image analysis method with a Berkovich indenter.

Indentation depth: 300 nm		
Sample	Method	Hardness [GPa]
AP	CSM	0.60 ± 0.08
	Image analysis	0.51 ± 0.11
HT	CSM	4.72 ± 0.62
	Image analysis	3.61 ± 0.48

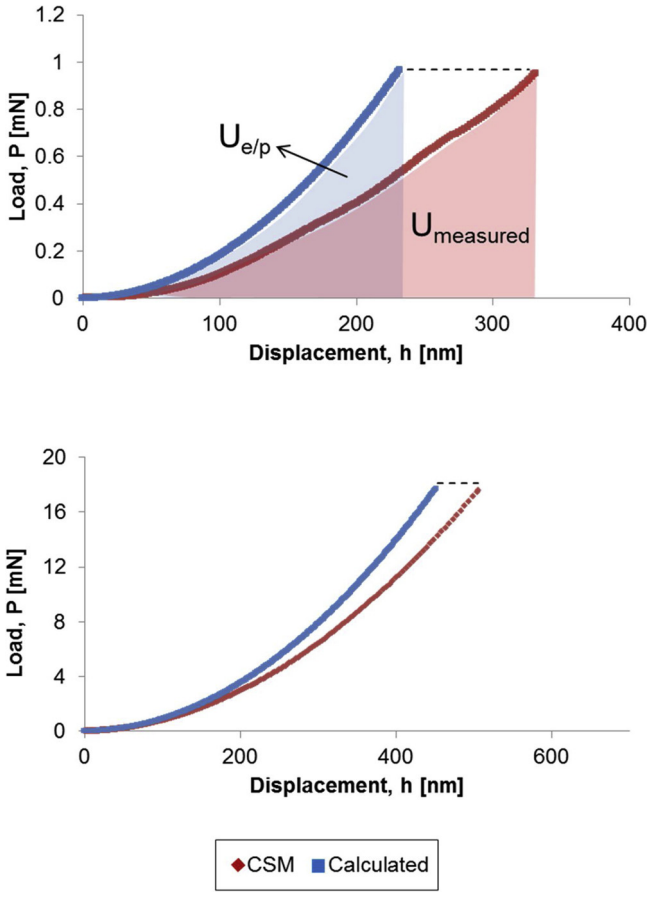

Fig. 6. Examples of calculated ideal elastoplastic curves for AP (upper) at HT (lower) material, with their corresponding measured CSM curves.

increase in fracture toughness, as one can immediately visualize by the generally shorter crack propagation path induced by the cube-corner indents in the HT material. The AP material also showed an overall larger number of cracks. The values obtained with the Anstis approach (Eq. 2) are almost 5-times lower than the ones obtained with the Laugier approach Eq. (4), because of the radically different assumptions as to the cracks' morphology induced by the cube-corner tip. This raises an open question as to which approach is most applicable for supercrystalline materials. FIB tomography and micro-computed tomography will be used in a follow-up of this study. In order to clarify such an ambiguity, fracture toughness was further investigated with a method alternative to ICL.

Table 2
Fracture toughness values obtained with the ICL method.

	K_{Ic} [MPa·m$^{1/2}$]	
	Anstis	Laugier
AP	0.14 ± 0.02	0.6 ± 0.1
HT	0.20 ± 0.01	1.2 ± 0.1

It is also worth mentioning explicitly that the ICL method only provides results for fracture toughness in Mode I (crack opening). However, the chipping phenomena that are typically affecting our supercrystalline materials are most likely related to fracture under shearing mode instead of crack opening, namely Mode II fracture, as inferred *via* SEM observations (Fig. 2). In order to evaluate the overall material's fracture toughness, together with the single cracking mode contributions, an energy-based method is adopted here [24]. This method is based on estimating the energy dissipated during irreversible cracking and chipping by comparing the measured load-displacement curves with the corresponding ideal elastoplastic ones, as described in the previous section (see Fig. 6).

We determine the critical energy release rate as [46]:

$$G_c = \frac{U_{e/p} - U_{measured}}{A} \tag{5}$$

with $U_{e/p}$ the energy associated with the calculated load-displacement curve of the ideal elastoplastic material, $U_{measured}$ the one relative to the experimental curve (CSM, cube-corner tip) and A the overall crack surface area.

The energy dissipation detected with the experimental curve, $U_{measured}$, takes into account all dissipation phenomena, including cracking and chipping. Therefore, the calculation of the crack area A needs to take both into account, and it requires some assumptions. The area A associated with chipping is measured with the image analysis software ImageJ of SEM images, as depicted in Fig. 8, neglecting their depth. As for the cracks propagating from the indents' corners, it was assumed that they would form either a quarter-penny shape or a Palmqvist form under the indent, as proposed by Cuadrado et al. [44,45], and calculations are thus conducted based on these two crack morphologies. This energy-based method was applied only to 300, 500 and 700 nm-deep indents, analogously to the ICL case. The following equation was then used to correlate the calculated critical energy rate to the fracture toughness [46]:

$$G_C = \frac{K_{Ic}^2}{E} + \frac{K_{IIc}^2}{E} + \frac{K_{IIIc}^2}{E(1-\nu)} \tag{6}$$

Here, E is the elastic modulus of the material and ν is the Poisson's ratio.

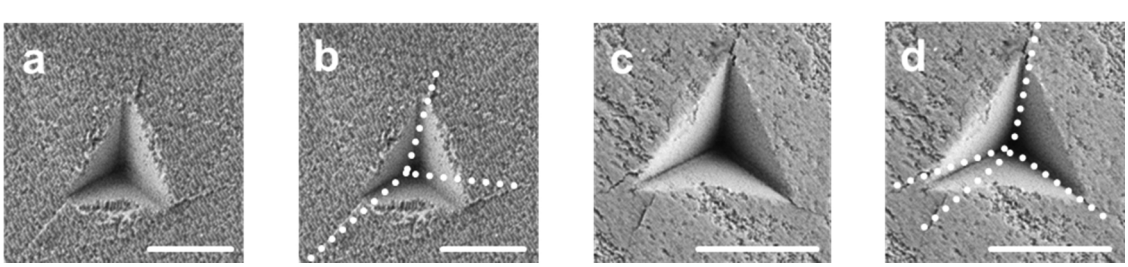

Fig. 7. Indentation-induced crack length measurement for CC indents: (a) AP 300 nm and (c) HT 500 nm. (b) and (d) show the crack length measurement of (a) and (c), respectively. Scale bar is 1 µm.

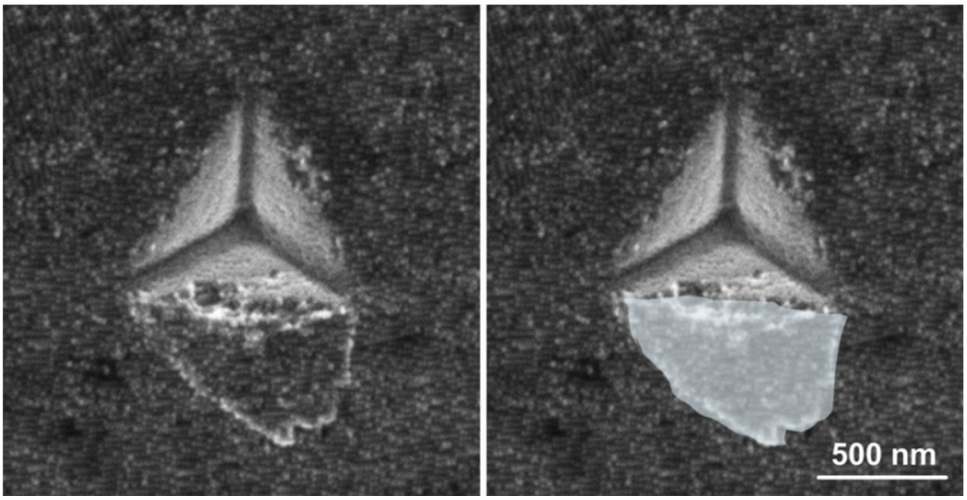

Fig. 8. Examples of chipped areas evaluation (AP material, CC 300 nm-deep indent).

K_{Ic}, K_{IIc} and K_{IIIc} are the fracture toughness values for opening, sliding and tearing modes, respectively. According to our working hypothesis, K_{Ic} is associated with radial cracks propagating from the indents' corners and K_{IIc} with the chips, while K_{IIIc} is assumed to be zero. Note also that any kinetic energy contribution was not taken into consideration in the present treatment.

Before proceeding to the calculation of K_{Ic} and K_{IIc} with this approach, the method was validated for K_{Ic} only. The validation consisted in considering the same indents used for the ICL study (radial cracks only) and applying Eq. (6) for the case in which K_{Ic} is the only term on the right-hand side that does not vanish.

Table 3 shows the results of this validation step. As expected, assuming a Palmqvist crack configuration (smaller extension with respect to quarter penny) consistently leads to higher fracture toughness values. There is indeed fairly good agreement between the results obtained with ICL-Anstis and energy-quarter penny methods, and between the ones obtained with ICL-Laugier and energy-Palmqvist methods. The latter are, however, unrealistically high for a ceramic-organic nanocomposite showing such cracking and chipping behavior (Fig. 2), as the Barenblatt analysis presented below will also confirm. We thus consider the values generated using the ICL-Anstis and energy method-quarter penny crack to be the most reliable K_{Ic} estimate.

The energy method was then used to obtain fracture toughness under shear conditions, namely that associated with chipping phenomena, K_{IIc}, as

$$K_{IIc} = \sqrt{G_C E - {K_{Ic}}^2} \tag{7}$$

with K_{Ic} as estimated by means of ICL method with the Anstis equation. The outcomes are summarized in Table 4.

The obtained values of fracture toughness for opening and shearing mode (I and II, respectively) suggest that both cracking modes play a role in ceramic-organic supercrystalline nanocomposites, with or without heating-induced crosslinking. However, for a material in which the nanoscale building blocks are held together by weak interactions only (AP), a higher resistance to crack propagation under shearing mode is observed with respect to the opening mode. The expected increase in fracture toughness of the heat-treated material is observed.

Table 3
Validation of the energy-based method for fracture toughness evaluation.

Sample	Mean K_{IC} [MPa• $m^{1/2}$]			
	ICL		Energy method	
	Equation		Crack morphology	
	Anstis	Laugier	Quarter-penny	Palmqvist
AP	0.14 ± 0.02	0.6 ± 0.1	0.1 ± 0.1	0.4 ± 0.1
HT	0.21 ± 0.03	1.2 ± 0.1	0.5 ± 0.3	2.2 ± 0.8

Table 4
Fracture toughness values calculated with ICL and energy-based methods.

Sample	ICL	Energy method	
	K_{Ic} [MPa• $m^{1/2}$]	K_{Ic} [MPa• $m^{1/2}$]	K_{IIc} [MPa• $m^{1/2}$]
AP	0.14 ± 0.02	0.1 ± 0.1	0.4 ± 0.2
HT	0.21 ± 0.03	0.5 ± 0.3	0.7 ± 0.1

The fracture toughness for the HT material could also be estimated by means of a Barenblatt approach [30,47]. It is assumed that the material's toughness, G_{Ic}, is due to the bridging force F between the nanoparticles, as

$$G_{Ic} = \rho_{cl} \int_0^{u_c} F\, du \tag{8}$$

where ρ_{cl} is the area fraction of crosslinked bonds and u is the displacement between the nanoparticles measured with respect to their equilibrium position. In the purely elastic regime case, the bonds break at a critical value u_c.

It was shown, using ultrahigh vacuum infrared reflection absorption spectroscopy (UHV-IRRAS) and X-ray photon spectroscopy (XPS), that the oleic acid molecules are crosslinked after heat treatment, and that they are attached to the magnetite nanoparticles *via* their carboxylic group [14]. We therefore assumed that their conformational freedom is reduced almost to zero, which means that they behave in a linear elastic fashion. A linear elastic nanocomposite model based on a DFT calculation on alkanes [47] was indeed able to describe the elastic properties of the composites, as well as their strength [14]. We apply here the same linear elastic model for the oleic acid molecules [46], leading to the following the load-displacement relationship:

$$F = k\,u, \quad \text{for } u < u_c \tag{9}$$

where k is the spring constant of the bond and u_c is the critical displacement value, corresponding to the breakage of a bond in the oleic acid molecule or to the detachment of the carboxylic group from the surface of the iron oxide. F_c is the respective force. From Eqs. (8) and (9), we have:

$$G_{Ic} = \frac{\rho_{cl} F_c^2}{2k} \tag{10}$$

Finally, by applying Eq. (6), we obtain:

$$K_{Ic} = \sqrt{\frac{E\,\rho_{cl}F_c^{\,2}}{2\,k}} \tag{11}$$

As an estimate for the spring constant, we use the result from [47], $k = \frac{28.7\,nN}{1\,nm} \cong 29\,\frac{N}{m}$. We then assume interdigitated oleic acid molecules with a nearest neighbor particle distance of 1 nm, leading to a crosslink density $\rho_{cl} = 0.33\frac{1}{nm^2}$, and the value for the breaking force $F_c = 1.4$ nN [14]. Finally, we use the elastic modulus determined in this investigation, $E = 64.1$ GPa. Introducing these values in Eq. (11) leads to a fracture toughness of $0.03\,MPa\sqrt{m}$. This result predicts a fracture toughness that is six times smaller than the one measured with the ICL – method.

We therefore conclude that the fracture toughness of the HT nanocomposites cannot be due only to the breaking of the crosslinking bonds between the ligand chains. There must be extrinsic toughening processes playing a role, which are probably the classical mechanisms operating in brittle materials, such as crack deflection and bridging. Indeed, because of the super-crystallographic nature and the consequent anisotropy of our material, the ideal indentation cracks – stemming from indents' corners and following a straight path – were never observed. The cracks had different lengths at each corner of the same indent and they deviated following a tortuous path. Fig. 9 shows an example of crack deflection through supercrystalline planes. Plastic deformation might also contribute to the fracture toughness of the supercrystals, and such a phenomenon is the object of ongoing investigations.

Our analysis of elastic modulus, hardness and fracture toughness in AP and HT bulk supercrystalline nanocomposites suggests that there is a notable difference in the deformation mechanisms and mechanical response of the two materials when using Berkovich and cube-corner indenters in CSM-mode.

For the AP material, it is likely that the sharper cube-corner tip leads to significant compaction underneath the indent, whereas for the Berkovich case this effect is much less pronounced. This compaction leads to a stiffer and harder AP material. Micromechanically the compaction is probably due to the non-linear displacement of the organic ligands into the interstitials sites of the FCC structure. These tetrahedral and octahedral interstitials are empty, because the solvent molecules that originally occupied them evaporated during the vacuum drying process. The Berkovich indenter is much less sharp and thus causes only minor compaction effects. Nevertheless, it is very likely that both indenters induce shear processes underneath the indent which may result in dislocations or twinning. A detailed transmission electron microscopy analysis of these processes is beyond the scope of the present article and will be discussed in another study.

For the HT supercrystalline material the crosslinking of the bonds reduces not only the nanoparticles' freedom of rearrangement, but also the non-linear displacements of the ligands, and therefore additional compaction of the supercrystals is more limited. On the other hand, the much higher stresses induced by the sharp cube-corner indenter are most likely beyond the fracture stress of the crosslinked ligands, and thus deformation can be induced by very localized cracking of the crosslinks, followed by local shearing. This process is much less pronounced when a Berkovich indenter is applied. Therefore, the hardness and elastic modulus results measured with the Berkovich indentation tip reflect more accurately the real properties of bulk supercrystalline materials.

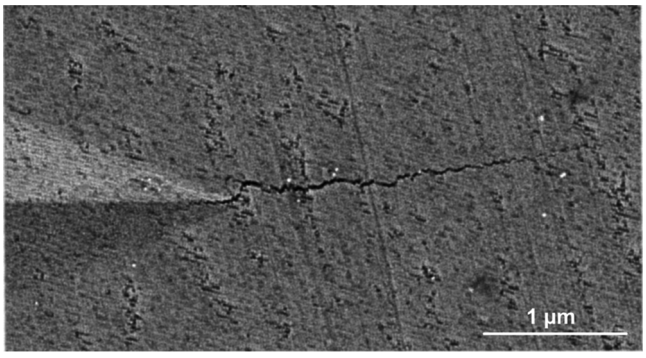

Fig. 9. Crack path deflection at the corner of a 1000-nm deep Berkovich indent in the HT material.

It is also worth noting that, since all indentation tests were performed in CSM-mode, an effect of the displacement modulation of the indenter cannot be excluded. This could lead to a softening effect, especially in the AP case, showing non-linear deformation processes that could be attributed to a viscoelastic response of the material or to a reduction of the yield stress due to plastic deformation. The influence of the oscillations characterizing the CSM indentation method will be investigated in a separate study.

4. Conclusions

In this study the elastic modulus, hardness and fracture toughness of bulk poly-supercrystalline nanocomposites of oleic acid-functionalized iron oxide nanoparticles were investigated. The underlying micromechanical deformation mechanisms were analyzed for the first time, for materials with and without crosslinking of the organic ligands. The two indenter tips adopted in the study, cube-corner and Berkovich, measured different elastic modulus and hardness in CSM-mode. The analysis of the SEM images of the indents and the load-displacement curves revealed that both Berkovich and cube-corner indenters lead to compaction, cracking and chipping of the nanocomposites. However, as the Berkovich tip induces a more hydrostatic deformation, these processes become less pronounced, and therefore the Berkovich-measured elastic modulus and hardness are closer to the intrinsic properties of the material. The proposed densification model and the effect of indentation methods alternative to CSM are the focus of ongoing follow-up work. As the cracking and chipping phenomena are minimized at the lowest indentation depths, we consider as most accurate hardness and elastic modulus values the ones generated with the Berkovich indenter and penetrating to only 300-nm depth, *i.e.* $E = 14.8 \pm 1.1$ GPa and $H = 0.60 \pm 0.08$ GPa for the AP material, and $E = 64.1 \pm 5.8$ and $H = 4.72 \pm 0.62$ for the HT material. A fracture toughness study for bulk supercrystalline materials was also performed, resulting in values of $K_{Ic} = 0.14\,MPa \cdot m^{1/2}$ for the AP material and $K_{Ic} = 0.2\,MPa \cdot m^{1/2}$ for the HT material. Distinct K_{Ic} outcomes obtained with different models for the ICL method showed that it is not trivial to select the appropriate equations without having insights as to the crack morphology under the indents. A first-of-a-kind energy-based fracture toughness approach is also applied, stressing again the importance of the crack path shape, and providing an estimation of the material's resistance to crack propagation for Mode II (sliding). A Barenblatt-type analysis of the fracture toughness based on the ligands' covalent bonding reveals that the intrinsic fracture toughness of the supercrystals is much smaller than the measured one. Hence, extrinsic contributions to the material's resistance to crack propagation, such as the development of a plastic zone, microcracking or crack deflection, are necessarily playing a role in these crosslinked supercrystals. Future work will be directed towards a more detailed understanding of the underlying dislocation or twinning mechanisms leading to plastic deformation.

Acknowledgements

The authors gratefully acknowledge financial support from the Deutsche Forschungsgemeinschaft (DFG, German Research Foundation) – Projektnummer 192346071 – SFB 986. B.B. gratefully acknowledges the support from the Ministry of National Education of the Republic of Turkey. D.G. gratefully acknowledges the support from the Alexander von Humboldt Foundation. The authors are very thankful to Prof. Erica Lilleodden for the stimulating discussions and valuable input provided

during the course of this study, and to Dr. Tobias Krekeler and Dr. Martin Ritter for their assistance with imaging of the samples.

References

[1] C.-W. Liao, Y.-S. Lin, K. Chanda, Y.-F. Song, M.H. Huang, Formation of diverse supercrystals from self-assembly of a variety of polyhedral gold nanocrystals, J. Am. Chem. Soc. 135 (2013) 2684–2693.

[2] P. Podsiadlo, G. Krylova, B. Lee, K. Critchley, D.J. Gosztola, et al., The role of order, nanocrystal size, and capping ligands in the collective mechanical response of three-dimensional nanocrystal solids, J. Am. Chem. Soc. 132 (2010) 8953–8960.

[3] H. Cölfen, M. Antonietti, Mesocrystals: Inorganic superstructures made by highly parallel crystallization and controlled alignment, Angew. Chem. Int. Ed. Engl. 44 (2005) 5576–5591.

[4] Elena V. Sturm, Helmut Cölfen, Mesocrystals: Past, Presence, Future, Crystals 7 (2017) 207.

[5] M.A. Boles, M. Engel, D.V. Talapin, Self-assembly of colloidal nanocrystals: from intricate structures to functional materials, Chem. Rev. 116 (2016) 11220–11289.

[6] D.V. Talapin, J.-S. Lee, M.V. Kovalenko, E.V. Shevchenko, Prospects of colloidal nanocrystals for electronic and optoelectronic applications, Chem. Rev. 110 (2010) 389–458.

[7] Z. Liu, M.A. Meyers, Z. Zhang, R.O. Ritchie, Functional gradients and heterogeneities in biological materials: design principles, functions, and bioinspired applications, Prog. Mater. Sci. 88 (2017) 467–498.

[8] P.H.C. Camargo, K.G. Satyanarayana, F. Wypych, Nanocomposites: synthesis, structure, properties and new application opportunities, Mat. Res. 12 (2009) 1–39.

[9] E. Munch, M.E. Launey, D.H. Alsem, E. Saiz, A.P. Tomsia, et al., Tough, bio-inspired hybrid materials, Science 322 (2008) 1516–1520.

[10] U.G.K. Wegst, H. Bai, E. Saiz, A.P. Tomsia, R.O. Ritchie, Bioinspired structural materials, Nat. Mater. 14 (2015) 23–36.

[11] A.R. Studart, Towards high-performance bioinspired composites, Adv. Mater. Weinheim 24 (2012) 5024–5044.

[12] F. Bouville, E. Maire, S. Meille, B. van de Moortèle, A.J. Stevenson, et al., Strong, tough and stiff bioinspired ceramics from brittle constituents, Nat. Mater. 13 (2014) 508–514.

[13] H.-L. Gao, S.-M. Chen, L.-B. Mao, Z.-Q. Song, H.-B. Yao, et al., Mass production of bulk artificial nacre with excellent mechanical properties, Nat. Commun. 8 (2017) 287.

[14] A. Dreyer, A. Feld, A. Kornowski, E.D. Yilmaz, H. Noei, et al., Organically linked iron oxide nanoparticle supercrystals with exceptional isotropic mechanical properties, Nat. Mater. 15 (2016) 522–528.

[15] E. Tam, P. Podsiadlo, E. Shevchenko, D.F. Ogletree, M.-P. Delplancke-Ogletree, et al., Mechanical properties of face-centered cubic supercrystals of nanocrystals, Nano Lett. 10 (2010) 2363–2367.

[16] X.W. Gu, X. Ye, D.M. Koshy, S. Vachhani, P. Hosemann, et al., Tolerance to structural disorder and tunable mechanical behavior in self-assembled superlattices of polymer-grafted nanocrystals, Proc. Natl. Acad. Sci. U. S. A. 114 (2017) 2836–2841.

[17] X. Qin, D. Luo, Z. Xue, Q. Song, T. Wang, Self-assembled Ag-MXA superclusters with structure-dependent mechanical properties, Adv. Mater. Weinheim 30 (2018).

[18] M. Gauvin, N. Yang, E. Barthel, I. Arfaoui, J. Yang, et al., Morphology, Nanocrystallinity, and Elastic Properties of Single Domain ε-Co Supracrystals, J. Phys. Chem. C 119 (2015) 7483–7490.

[19] M.P. Pileni, Supra- and nanocrystallinity: Specific properties related to crystal growth mechanisms and nanocrystallinity, Acc. Chem. Res. 45 (2012) 1965–1972.

[20] N. Goubet, J. Richardi, P.-A. Albouy, M.-P. Pileni, Which Forces Control Supracrystal Nucleation in Organic Media? Adv. Funct. Mater. 21 (2011) 2693–2704.

[21] P. Podsiadlo, B. Lee, V.B. Prakapenka, G.V. Krylova, R.D. Schaller, et al., High-pressure structural stability and elasticity of supercrystals self-assembled from nanocrystals, Nano Lett. 11 (2011) 579–588.

[22] D.S. Harding, W.C. Oliver, G.M. Pharr, Cracking During Nanoindentation and its Use in the Measurement of Fracture Toughness, MRS Proc. 356 (1994) 15.

[23] Y.-T. Cheng, C.-M. Cheng, Relationships between hardness, elastic modulus, and the work of indentation, Appl. Phys. Lett. 73 (1998) 614–616.

[24] J. Malzbender, G. With de, Energy dissipation, fracture toughness and the indentation load–displacement curve of coated materials, Surf. Coat. Technol. 135 (2000) 60–68.

[25] A. Leitner, V. Maier-Kiener, D. Kiener, Extraction of Flow Behavior and Hall-Petch Parameters Using a Nanoindentation Multiple Sharp Tip Approach, Adv. Eng. Mater. 19 (2017) 1600669.

[26] K. Durst, O. Franke, A. Böhner, M. Göken, Indentation size effect in Ni–Fe solid solutions, Acta Mater. 55 (2007) 6825–6833.

[27] G.M. Pharr, J.H. Strader, W.C. Oliver, Critical issues in making small-depth mechanical property measurements by nanoindentation with continuous stiffness measurement, J. Mater. Res. 24 (2009) 653–666.

[28] M.J. Cordill, M.S. Lund, J. Parker, C. Leighton, A.K. Nair, et al., The Nano-Jackhammer effect in probing near-surface mechanical properties, Int. J. Plast. 25 (2009) 2045–2058.

[29] Y.-F. Jia, Y.-Y. Cui, F.-Z. Xuan, F. Yang, Comparison between single loading–unloading indentation and continuous stiffness indentation, RSC Adv. 7 (2017) 35655–35665.

[30] G.I. Barenblatt, The mathematical theory of equilibrium cracks in brittle fracture, in: H.L. Dryden, Karman T. von (Eds.), Advances in Applied Mechanics, vol. 7, Academic P, New York, 1962, pp. 55–129.

[31] W.C. Oliver, G.M. Pharr, Measurement of hardness and elastic modulus by instrumented indentation: advances in understanding and refinements to methodology, J. Mater. Res. 19 (2004) 3–20.

[32] C.A. Schneider, W.S. Rasband, K.W. Eliceiri, NIH Image to ImageJ: 25 years of image analysis, Nat. Methods 9 (2012) 671–675.

[33] C.A. Schuh, Nanoindentation studies of materials, Mater. Today 9 (2006) 32–40.

[34] S. Amini, M. Tadayon, S. Idapalapati, A. Miserez, The role of quasi-plasticity in the extreme contact damage tolerance of the stomatopod dactyl club, Nat. Mater. 14 (2015) 943–950.

[35] W.C. Oliver, G.M. Pharr, An improved technique for determining hardness and elastic modulus using load and displacement sensing indentation experiments, J. Mater. Res. 7 (1992) 1564–1583.

[36] G.R. Anstis, P. Chantikul, B.R. Lawn, D.B. Marshall, A critical evaluation of indentation techniques for measuring fracture toughness: I, direct crack measurements, J. Am. Ceram. Soc. 64 (1981) 533–538.

[37] M.T. Laugier, New formula for indentation toughness in ceramics, J. Mater. Sci. Lett. 6 (1987) 355–356.

[38] B.R. Lawn, A.G. Evans, D.B. Marshall, Elastic/Plastic indentation damage in ceramics: the Median/Radial crack system, J. Am. Ceram. Soc. 63 (1980) 574–581.

[39] B.R. Lawn, D.B. Marshall, Hardness, toughness, and brittleness: an indentation analysis, J. Am. Ceram. Soc. 62 (1979) 347–350.

[40] R.D. Dukino, M.V. Swain, Comparative Measurement of Indentation Fracture Toughness with Berkovich and Vickers Indenters, J. Am. Ceram. Soc. 75 (1992) 3299–3304.

[41] T. Scholz, G.A. Schneider, J. Muñoz-Saldaña, M.V. Swain, Fracture toughness from submicron derived indentation cracks, Appl. Phys. Lett. 84 (2004) 3055–3057.

[42] D.J. Morris, R.F. Cook, In situ cube-corner indentation of soda-lime glass and fused silica, J. Am. Ceram. Soc. 87 (2004) 1494–1501.

[43] A. Miserez, J.C. Weaver, P.J. Thurner, J. Aizenberg, Y. Dauphin, et al., Effects of Laminate Architecture on Fracture Resistance of Sponge Biosilica: Lessons from Nature, Adv. Funct. Mater. 18 (2008) 1241–1248.

[44] N. Cuadrado, D. Casellas, M. Anglada, E. Jiménez-Piqué, Evaluation of fracture toughness of small volumes by means of cube-corner nanoindentation, Scr. Mater. 66 (2012) 670–673.

[45] N. Cuadrado, J. Seuba, D. Casellas, M. Anglada, E. Jiménez-Piqué, Geometry of nanoindentation cube-corner cracks observed by FIB tomography: Implication for fracture resistance estimation, J. Eur. Ceram. Soc. 35 (2015) 2949–2955.

[46] B. Lawn, Fracture of Brittle Solids, 2nd ed., Cambridge Univ. Press, Cambridge, 1998.

[47] T. Hugel, M. Rief, M. Seitz, H.E. Gaub, R.R. Netz, Highly stretched single polymers: atomic-force-microscope experiments versus ab-initio theory, Phys. Rev. Lett. 94 (2005) 48301.